

Adaptive Subarray Segmentation: A New Paradigm of Spatial Non-Stationary Near-Field Channel Estimation for XL-MIMO Systems

Shuhang Yang, *Graduate Student Member, IEEE*, Puguang An, Peng Yang, *Member, IEEE*, Xianbin Cao, *Senior Member, IEEE*, Dapeng Oliver Wu, *Fellow, IEEE*, and Tony Q. S. Quek, *Fellow, IEEE*

Abstract—To tackle the complexities of spatial non-stationary (SnS) effects and spherical wave propagation in near-field channel estimation (CE) for extremely large-scale multiple-input multiple-output (XL-MIMO) systems, this paper introduces an innovative SnS near-field CE framework grounded in adaptive subarray partitioning. Conventional methods relying on equal subarray partitioning often lead to suboptimal divisions, undermining CE precision. To overcome this, we propose an adaptive subarray segmentation approach. First, we develop a spherical-wave channel model customized for line-of-sight (LoS) XL-MIMO systems to capture SnS traits. Next, we define and evaluate the adverse effects of over-segmentation and under-segmentation on CE efficacy. To counter these issues, we introduce a novel dynamic hybrid beamforming-assisted power-based subarray segmentation paradigm (DHBF-PSSP), which merges cost-effective power measurements with a DHBF structure, enabling joint subarray partitioning and decoupling. A robust partitioning algorithm, termed power-adaptive subarray segmentation (PASS), exploits statistical features of power profiles, while the DHBF utilizes subarray segmentation-based group time block code (SS-GTBC) to enable efficient subarray decoupling with limited radio frequency (RF) chain resources. Additionally, by utilizing angular-domain block sparsity and inter-subcarrier structured sparsity, we propose a subarray segmentation-based assorted block sparse Bayesian learning algorithm under the multiple measurement vectors framework (SS-ABSBL-MMV), employing discrete Fourier transform (DFT) codebooks to lower complexity. Extensive simulation results validate the exceptional performance of the proposed framework over its counterparts.

Index Terms—Spatial non-stationary, near-field, channel estimation, dynamic hybrid beamforming, block sparsity

I. INTRODUCTION

TO meet the ever-growing communication capacity demands of 6G networks, communication systems are shifting towards millimeter-wave (mmWave) and terahertz (THz) frequencies [1]. Due to the high path loss and short wavelength of high-frequency signals, the combination of extremely large-scale multiple-input multiple-output (XL-MIMO) and mmWave/THz technology enhances gain and spectral efficiency while maintaining a limited antenna size [2]. However, as the number of antennas increases dramatically, the Rayleigh

distance of the array shrinks significantly, causing user equipment (UE) to potentially fall within the radiative near-field region. In this region, electromagnetic wave propagation is better approximated by a spherical wave model rather than the conventional plane wave assumption [3]. Additionally, the massive number of elements in XL-MIMO arrays allows different array regions to observe distinct scatterers, leading to the spatial non-stationary (SnS) effect [4], [5]. Channel state information (CSI) acquisition is crucial for optimizing wireless communication systems. However, due to the large number of elements and the impact of SnS in XL-MIMO systems, achieving high-accuracy CE with low pilot overhead remains a significant challenge. This paper is concerned with the SnS near-field CE for XL-MIMO systems.

A. Prior Works

Near-field channel estimation: Under the far-field plane-wave assumption, exploiting the angular-domain sparsity of the mmWave/THz channel, numerous compressive sensing (CS) algorithms have been employed for CE with low pilot overhead. These include the well-known orthogonal matching pursuit (OMP) algorithm [6], sparse Bayesian learning (SBL) [7], variational Bayesian inference (VBI) algorithm [8], and approximate message passing (AMP) algorithm [9]. To address the on-grid mismatch issue, [10] and [11] proposed the iterative reweighted super-resolution compressive sensing approach and the atomic norm minimization-based gridless compressive sensing algorithm, respectively.

Under the near-field spherical-wave assumption, the inherent nonlinear coupling between distance and angle in the steering vector invalidates conventional far-field CE methods. To address this, the authors in [12] introduced a polar-domain codebook that jointly samples distance and angle, along with an on/off-grid simultaneous OMP (SOMP) algorithm. However, this two-dimensional (2D) sampling generates a large-scale sparsifying dictionary, leading to high computational complexity. Additionally, the strong correlation among near-field steering vectors degrades the restricted isometry property (RIP), further limiting CE performance. Building on this, [13] proposed a distance-parameterized angular-domain sparse model, where user distance is incorporated as an unknown parameter in the dictionary. In contrast to distance-angle representations, [14] developed a beam-delay spatial-frequency domain channel characterization method and employed a

S. Yang, P. An, P. Yang, and X. Cao are with the School of Electronic and Information Engineering, Beihang University, Beijing 100191, China.

D. O. Wu is with the Department of Computer Science, City University of Hong Kong, Kowloon, Hong Kong, China.

T. Q. S. Quek is with the Information Systems Technology and Design Pillar, Singapore University of Technology and Design, Singapore 487372, Singapore.

hybrid message passing (HMP) algorithm to recover sparse channel parameters. Separately, [15] designed a discrete prolate spheroidal sequence (DPSS)-based codebook and a two-step CE scheme, though it requires prior rough UE location estimation. Differing from these approaches, [16] explored the block sparsity shared between near-field and far-field angular domains and proposed a complex simultaneous logit-weighted block OMP (CSLW-BOMP) algorithm to exploit this structural characteristic.

XL-MIMO channel estimation affected by SnS: In XL-MIMO systems, most existing SnS near-field CE methods involve partitioning the array equally into multiple subarrays and conducting CE for each subarray individually [17]–[20]. To address the subarray coupling issue under limited radio frequency (RF) chains, the authors in [17] proposed a group time block code (GTBC)-assisted subarray decoupling method in a fully connected hybrid beamforming (HBF) architecture. However, this architecture requires a large number of pilots to decouple subarrays. In contrast, [21] conducted a 2D Markov prior model to capture the visibility region (VR), and then performed CE based on inverse-free VBI (IF-VBI). The two-stage VR detection and CE scheme was also adopted in [22], but it leveraged the sparsity in the wavenumber domain. However, these two-stage schemes critically depend on accurate prior modeling. Moreover, applying masking operations to the original polar-domain codebook may further deteriorate the performance of codebooks that already suffer from inherent limitations. Unlike the approach of modeling the prior of the VR, in [23], the VR of the user was identified by exploiting the statistical characteristic of the received power across the antenna elements. Although this statistical characteristic depends on the accuracy of CE and needs a great improvement in low signal-to-noise ratio (SNR) conditions, it still offers us a new perspective.

B. Our Contributions

Considering the issues in existing research about SnS near-field CE, this paper proposes a method from the perspective of adaptive subarray partitioning, exploiting the block sparsity in the near-field angular domain. The main contributions are summarized as follows.

- This paper first develops a spherical-wave channel model for near-field XL-MIMO systems with line-of-sight (LoS) propagation, specifically analyzing the SnS characteristics in this scenario. Based on fundamental spherical wave assumptions, the proposed model incorporates non-ideal LoS paths in obstructed-LoS (OLOs) scenarios and applies VR-based weighting masks to the original spatial channel matrix to capture SnS effects.
- This paper proposes the concepts of over-segmentation and under-segmentation as non-ideal subarray partitioning modes, theoretically analyzing their negative effects on CE to expose limitations of existing CE methods relying on equal subarray division. To overcome these challenges, a novel framework integrating low-cost power measurements with a dynamic hybrid beamforming (DHBF) architecture is introduced for joint subarray

partitioning and decoupling. Specifically, a robust partitioning algorithm is designed by exploiting the statistical properties of measured power profiles. Additionally, under limited RF chain resources, the DHBF architecture is synergized with subarray segmentation-based GTBC (SS-GTBC) to achieve effective subarray decoupling.

- Based on the subarrays obtained after the aforementioned array partitioning, by leveraging the block sparsity in the angular domain of the near-field channel and the structured sparsity among subcarriers, this paper proposes a subarray segmentation-based assorted block sparse bayesian learning under the multiple measurement vectors framework (SS-ABSBL-MMV) to perform CE for each sub-channel and develops two versions: on-grid and off-grid. Moreover, even though this scheme employs a discrete Fourier transform (DFT) codebook with significantly fewer atoms than the polar-domain codebook, it still achieves remarkable CE performance.

C. Organization and Notations

Organization: The rest of this paper is organized as follows. In Section II, we present the SnS near-field channel model for LoS XL-MIMO systems. Subsequently, in Section III, we derive and elaborate on the importance of precise array partitioning, proposing the DHBF-PSSP and validating its effectiveness. In Section IV, we provide a detailed description of the SS-ABSBL-MMV algorithm. In Section V, simulation results are presented and analyzed, followed by the conclusion in Section VI.

Notations: Lowercase and uppercase bold letterers denote vectors and matrices, respectively. Let $(\cdot)^{-1}$, $(\cdot)^T$, $(\cdot)^H$, $\|\cdot\|$, $\text{vec}(\cdot)$, $\det(\cdot)$, represent the inverse, transpose, conjugate transpose, ℓ_2 -norm, vectorization, and determinant, respectively. $\text{diag}(\cdot)$ is used to extract diagonal elements from a matrix or to construct a matrix with a vector as its diagonal elements. \otimes is the Kronecker product operator and \odot means the Hadamard product operator. $\Re\{\cdot\}$ denote the real part of the complex argument. \mathbf{I}_N is the $N \times N$ dimensional identity matrix, and $\mathbf{1}_{M \times N}$ is the $M \times N$ dimensional all-one matrix. For a set, $|\cdot|$ denotes the cardinality of the set. $\mathcal{CN}(\mathbf{x}; \boldsymbol{\mu}, \boldsymbol{\Sigma})$ denotes the complex Gaussian distribution with mean $\boldsymbol{\mu}$ and covariance $\boldsymbol{\Sigma}$.

II. SNS NEAR-FIELD CHANNEL MODEL

A. Near-field Spherical Wave Channel Model

XL-MIMO systems employ large-scale antenna arrays with N elements at the base station (BS), where the increased aperture quadratically extends Rayleigh distances. This likely positions UEs in the BS's radiating near-field, requiring spherical wave models for channel characterization:

$$\mathbf{h} = \sum_{l=1}^L g_l e^{-j \frac{2\pi f}{c} r_l} \cdot \mathbf{b}(r_l, \theta_l), \quad (1)$$

where L denotes the number of propagation paths, g_l represents the complex channel gain of the l -th path. f and c denote the carrier frequency and the speed of light. r_l and

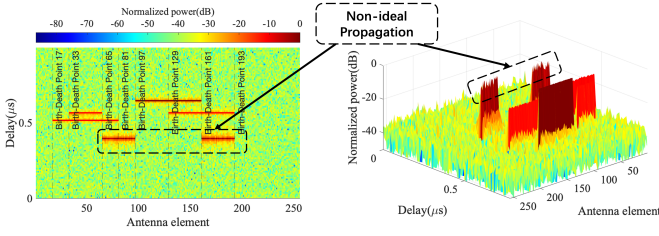


Fig. 1. Model-generated SnS near-field channel, with $N = 256$ antennas, $K = 4$ users, $M = 100$ subcarriers, SNR = 15 dB.

θ_l represent the distance and angular separation between the l -th scatterer/UE and the reference antenna, respectively. The near-field steering vector $\mathbf{b}(r_l, \theta_l)$ can be expressed as:

$$\mathbf{b}(r_l, \theta_l) = \frac{1}{\sqrt{N}} \left[e^{-jk(r_l^{(1)} - r_l)}, \dots, e^{-jk(r_l^{(N)} - r_l)} \right]^T, \quad (2)$$

where $r_l^{(n)}$ denotes the distance between the l -th scatterer/UE and the n -th antenna element. And $k = 2\pi f/c$ denotes the wavenumber. Based on the geometric relationship and Taylor expansion, it can be approximated as:

$$r_l^{(n)} \approx r_l - \Delta_n d r_l \sin \theta_l + \frac{(\Delta_n d \cos \theta_l)^2}{2r_l}, \quad (3)$$

where d represents the antenna spacing, which is typically set as $d = \lambda/2$ (half-wavelength spacing). And $\Delta_n = \frac{2n-N-1}{2}$, $n = 1, 2, \dots, N$.

Observing the above formula, the near-field steering vector $\mathbf{b}(r_l, \theta_l)$ exhibits a nonlinear phase-antenna index relationship due to additional nonlinear terms. Notably, when r_l increases, these nonlinear terms diminish, and the model reduces to the far-field plane wave approximation.

Furthermore, considering the limited diffraction and severe path loss in millimeter-wave environments, the multipath propagation effects are relatively weak. Under low SNR conditions, non-LoS (NLoS) components become difficult to detect effectively [24], [25]. Therefore, this paper primarily focuses on the LoS path, i.e., the LoS XL-MIMO system [26], where the channel model can be simplified as:

$$\mathbf{h}_{\text{LoS}} = g_{\text{LoS}} \cdot e^{-j\frac{2\pi f}{c} r_{\text{LoS}}} \cdot \mathbf{b}(r_{\text{LoS}}, \theta_{\text{LoS}}). \quad (4)$$

B. SnS and its Impact

In XL-MIMO systems, due to the large array aperture that spans hundreds of wavelengths in space, the SnS occurs. In XL-MIMO systems with LoS conditions, the SnS can be summarized into the following three aspects.

In the near-field, spherical wavefronts cause slight power variations across the array due to varying distances between the source and antenna elements [27]. Additionally, the array's extensive spatial coverage results in partial blocking of some LoS paths, creating obstructed LoS (OLOs) scenarios where users can only access a subset of antennas, defined as the VR at the base station (BS-VR), with significantly higher signal power within this region. Furthermore, in these OLOs scenarios, diffraction at obstacle edges generates paths that share the similar time delays, AoAs, and BS-VR as the LoS

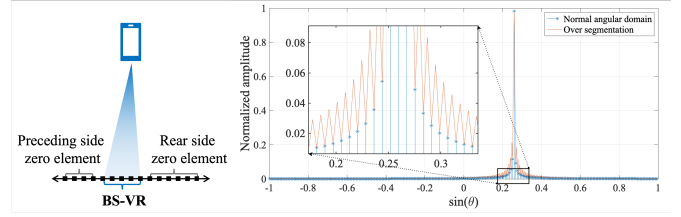


Fig. 2. Effect of over-segmentation on angular-domain channel.

path but exhibit spatially fluctuating power distributions due to diffraction effects [27], [28]. The combination of these diffracted paths with the LoS path leads to observable power fluctuations within the BS-VR.

Considering these factors, we propose an enhanced channel model that extends the conventional LoS XL-MIMO framework to support the SnS scenario. The modified channel model is expressed as:

$$\mathbf{h} = g_{\text{LoS}} \cdot e^{-j\frac{2\pi f}{c} r_{\text{LoS}}} \cdot \mathbf{b}(r_{\text{LoS}}, \theta_{\text{LoS}}) \odot \mathbf{s}. \quad (5)$$

The SnS properties are characterized through element-wise weighted masking of the channel matrix via vector \mathbf{s} , with its elements defined as [29]:

$$s^{(n)} = \begin{cases} = 1, & n \in \text{BS} - \text{VR}, \text{ ideal propagation} \\ > 0, & n \in \text{BS} - \text{VR}, \text{ non-ideal propagation.} \\ = 0, & n \notin \text{BS} - \text{VR} \end{cases} \quad (6)$$

As shown in the above equation, for non-ideal propagation scenarios with diffraction, the weighting factor should be positive. In this paper, to control the impact of non-ideal propagation on the model, the weighting factor within the BS-VR under non-ideal propagation scenarios follows a truncated Gaussian distribution, i.e., $s^{(n)} \sim \mathcal{N}_{\text{trunc}}(1, \sigma_s^2, \underline{t}_s, \bar{t}_s)$. Therefore, according to the definition of the truncated Gaussian distribution, the variance σ_s^2 can be regarded as a parameter controlling the intensity of power fluctuations, while the truncation factors $\underline{t}_s, \bar{t}_s > 0$ control the lower and upper bounds of the power fluctuations, respectively.

To clearly illustrate the impact of the SnS characteristics, Fig. 1 presents a delay-antenna-power diagram generated by the aforementioned channel model. It shows the BS-VRs corresponding to the LoS paths of the four UEs across the entire antenna array, which is partitioned into 9 subarrays. The definition for subarray can be summarized as follows: within a continuous array interval, if the set of visible UEs remains consistent, this continuous array interval is regarded as a subarray, and each subarray can be considered a stationary interval (SI). It is worth noting that the LoS path under the non-ideal propagation indicated by the arrow shows significant power fluctuations within the corresponding BS-VRs.

III. SUBARRAY SEGMENTATION: THEORETICAL IMPORTANCE AND INNOVATIVE PARADIGM

Conventional CE methods can't capture SnS properties, thus degrading CE accuracy. While existing SnS CE techniques employ fixed-length subarray partitioning and individual estimation [17], [18], [30], they cannot suppress the occurrence of

SnS birth-death within the predefined subarrays. To overcome this, we propose adaptive subarray segmentation before CE, followed by tailored estimation per subarray to accommodate SnS birth-death dynamics.

A. The Importance of Subarray Segmentation

First, we will elucidate the significance of subarray segmentation for CE. For the sake of brevity, we will discuss two scenarios of non-ideal subarray segmentation, namely *over-segmentation* and *under-segmentation*.

1) *Over-segmentation*: Over-segmentation refers to the unnecessary segmentation at the positions of array elements where the birth-death of SnS does not occur. This non-ideal segmentation limits subarray element counts, compromising angular resolution and CE accuracy.

2) *Under-segmentation*: Under-segmentation occurs when necessary segmentation is omitted at array element positions experiencing SnS birth-death events. This non-ideal segmentation allows the SnS to further affect the angular domain, thereby negatively impacting CE. Taking the far-field single-path scenario as an example, the angular-domain channel can be obtained by transforming the spatial-domain channel:

$$\mathbf{h}_a(k) = \frac{1}{\sqrt{N}} \sum_{n=0}^{N-1} \mathbf{h}(n) e^{-j \frac{2\pi n}{N} k}, k = 0, \dots, N-1. \quad (7)$$

Assume the BS-VR for this path spans a contiguous subset of Q array elements, with zero elements (no signal reception) flanking both sides. When restricting analysis to the rear-side zeros and omitting segmentation there, let the rear side contain $(r-1)Q$ zeros. The channel matrix under these conditions becomes:

$$\vec{\mathbf{h}}(n) = \begin{cases} \mathbf{h}(n), & n = 0, \dots, Q-1 \\ 0, & n = Q, \dots, rQ-1 \end{cases}. \quad (8)$$

Then its corresponding angular-domain channel matrix can be written as:

$$\begin{aligned} \vec{\mathbf{h}}_a(k) &= \frac{1}{\sqrt{rQ}} \sum_{n=0}^{rQ-1} \vec{\mathbf{h}}(n) e^{-j \frac{2\pi n}{rQ} k} \\ &= \frac{1}{\sqrt{rQ}} \sum_{m=0}^{Q-1} \frac{\mathbf{h}_a(m)}{Q} \frac{1 - e^{-j 2\pi \frac{k}{r}}}{1 - e^{j \frac{2\pi}{Q} (m - \frac{k}{r})}}, \\ &k = 0, 1, \dots, rQ-1. \end{aligned} \quad (9)$$

Similarly, if there are $(r-1)Q$ zero elements preceding the BS-VR, the angular-domain channel can be expressed as $\overleftarrow{\mathbf{h}}_a(k) = e^{-j \frac{2\pi(r-1)}{r} k} \vec{\mathbf{h}}_a(k)$. Analysis shows that redundancy in the spatial-domain sequence causes interpolation in non-target regions of the angular domain, as depicted in Fig. 2. This is similar to how zero-padding in the time domain leads to frequency domain interpolation in digital signal processing. Although zero-padding can enhance spectral resolution and reduce the picket-fence effect in time-frequency transforms [31], such interpolation disrupts sparsity in the angular domain, severely degrading CS performance. Thus, precise segmentation of XL-MIMO arrays is critical for SnS near-field channels.

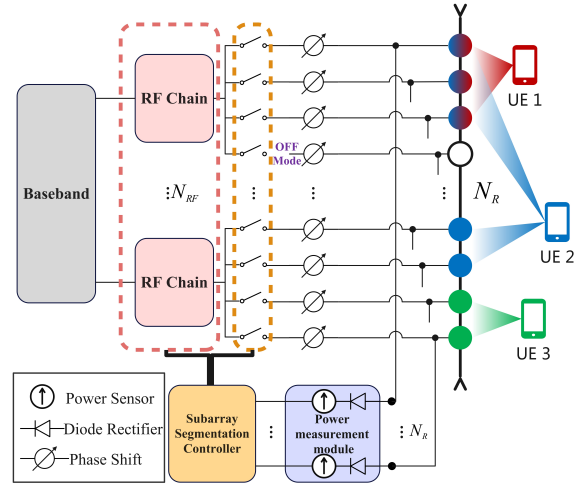


Fig. 3. Diagram of DHBF-PSSP.

B. DHBF-PSSP Overview

Before channel estimation, due to the limited features that can be extracted from the signal, signal power, as a readily measurable metric, serves as a key subarray partitioning criterion. Inter-subarray path variations induce distinct power statistics across subarrays, thereby enabling power-driven segmentation decisions.

Based on the analysis presented above, we propose an innovative subarray segmentation paradigm, termed the DHBF-assisted power-based subarray segmentation paradigm (DHBF-PSSP), as illustrated in Fig. 3.

- **Power Measurement and Subarray Partitioning:** Low-power (milliwatt-level) and cost-effective power sensors, as shown in [32], are deployed at the antenna end to measure the received power of each array element. Subarrays are then partitioned based on the measured power of each element, with the specific partitioning method detailed in the following subsection.
- **Application of DHBF Architecture:** The DHBF is used to enable adaptive subarray processing [4], [33]. This architecture offers the following advantages: (i) Subarrays are directly connected to their corresponding RF chains, and if there is no overlap among the RF chains used by different subarrays, no additional cost is incurred for subarray decoupling; (ii) When a subarray is detected to have insufficient power, it can be selectively deactivated, thereby effectively reducing RF power consumption. We refer to the deactivated subarrays as *off-mode*.
- **RF Chain Resource Allocation Strategy:** Given the constraint of a fixed number of RF chains, the following resource allocation strategy is adopted. When the number of active subarrays (excluding deactivated ones) is less than or equal to the number of RF chains, a direct connection approach is employed. When the number of active subarrays exceeds the number of RF chains, further refinement is required based on subarray decoupling using DHBF.

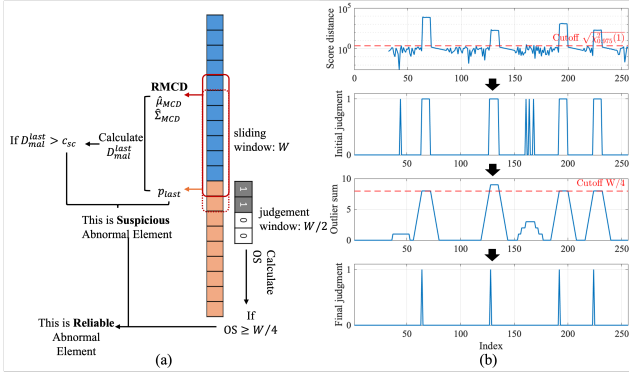


Fig. 4. PASS algorithm (a) Diagram of PASS, (b) Illustrative example of PASS steps.

C. Power-based Subarray Segmentation Algorithm

Inter-subarray discrepancies in multipath number and power induce pronounced statistical divergence in aggregate power. However, within a subarray, the spherical wave effect from multiple paths and the non-ideal propagation of some paths can lead to power fluctuations. These fluctuations, when combined with noise, may result in the under-segmentation between subarrays or the over-segmentation within a subarray.

Building on sequential change-point detection [34], this work recasts array partitioning as a change-point detection task via array power sequences. The received power distribution, however, remains analytically intractable due to spherical wavefronts and diffraction. Consequently, the proposed segmentation scheme requires: distribution-independent operation and computational efficiency.

Next, we will elaborate on a received-power-based subarray segmentation algorithm, termed the power-adaptive subarray segmentation (PASS) algorithm.

1) *PASS algorithm*: To capture the local statistical characteristics of the received power across the array, this paper adopts a sliding window detection method. A window of W array elements is defined, assuming the power distribution within the window (excluding abrupt changes) is approximately symmetric. This ensures that statistical quantities (e.g., mean and covariance) within the window effectively represent the array power distribution. By sliding the window along the array, the power of the last element in each position is tested for outliers.

To determine the outlyingness of the power of the last array element in the window relative to the power distribution within the window, the Mahalanobis distance is introduced:

$$D_{\text{mal}}^{\text{last}} = \sqrt{(p_{\text{last}} - \mu_w)^T \Sigma_w^{-1} (p_{\text{last}} - \mu_w)}, \quad (10)$$

where p_{last} represents the power value of the last array element in the window, μ_w and Σ_w denote the mean and variance within the window, respectively, and $D_{\text{mal}}^{\text{last}}$ is the Mahalanobis distance between p_{last} and the power distribution of the window. This distance is used as the score distance (SD) for p_{last} .

We utilize the reweighted minimum covariance determinant estimator (R-MCD) to estimate the mean and variance of the

power distribution within the window. The detailed implementation is as follows.

First, a subset of size h is selected within the window, where the window size satisfies $(W + 2)/2 \leq h \leq W$. Among all subsets of size h , the subset corresponding to the minimum determinant of the covariance matrix $\det(\Sigma_h)$ is chosen and denoted as \mathcal{H}_0 . The mean $\hat{\mu}_0$ and covariance matrix $\hat{\Sigma}_0$ of \mathcal{H}_0 are then computed:

$$\hat{\mu}_0 = \frac{1}{h} \sum_{i \in \mathcal{H}_0} p_i, \quad \hat{\Sigma}_0 = \frac{c_0}{h-1} \sum_{i \in \mathcal{H}_0} (p_i - \hat{\mu}_0)^2, \quad (11)$$

where $c_0 = \frac{h/W}{\mathbb{P}[\chi^2(3) < \chi_{h/n}^2(1)]}$ is a consistency factor.

Next, the initial estimates are reweighted as follows:

$$\hat{\mu}_{MCD} = \frac{\sum_{i=1}^W p_i I[d_i^2 < \chi_{0.975}^2(1)]}{\sum_{i=1}^W I[d_i^2 < \chi_{0.975}^2(1)]},$$

$$\hat{\Sigma}_{MCD} = \frac{c_1}{n-1} \sum_{i=1}^W I[d_i^2 < \chi_{0.975}^2(1)] \cdot (p_i - \hat{\mu}_{MCD})^2, \quad (12)$$

where $d_i = (p_i - \hat{\mu}_0) / \sqrt{\hat{\Sigma}_0}$, c_1 is a consistency factor, and $I(\cdot)$ is an indicator function. $\chi_{\alpha}^2(i)$ denotes the lower α -quantile of the chi-square distribution with i degrees of freedom (DoFs).

In summary, the SD is rewritten as:

$$D_{\text{mal}}^{\text{last}} = \sqrt{(p_{\text{last}} - \hat{\mu}_{MCD})^T \hat{\Sigma}_{MCD}^{-1} (p_{\text{last}} - \hat{\mu}_{MCD})}. \quad (13)$$

By incorporating the outlier discrimination threshold from robust principal component analysis (ROBPCA), the truncation threshold for the SD is set as $c_{\text{SD}} = \sqrt{\chi_{0.975}^2(1)}$. When $D_{\text{mal}}^{\text{last}} > c_{\text{SD}}$, the last array element in the current window is identified as a potential outlier. This threshold is derived from the fact: If $p_{\text{last}} \sim \mathcal{N}(\hat{\mu}_{MCD}, \hat{\Sigma}_{MCD})$, then $(D_{\text{mal}}^{\text{last}})^2 \sim \chi^2(1)$. Therefore, the rejection region $\mathcal{W}_0 = \{p_{\text{last}} \mid D_{\text{mal}}^{\text{last}} \geq \sqrt{\chi_{\alpha}^2(1)}\}$ can be defined to reject the hypothesis $p_{\text{last}} \sim \mathcal{N}(\hat{\mu}_{MCD}, \hat{\Sigma}_{MCD})$.

According to the aforementioned procedure, the window sequentially slides across the entire array and records the indices of all suspected anomalous elements, which are then transformed into a sequence $\{d_n\}_{n=1}^N$:

$$d_n = \begin{cases} 1, & n \in \{n : D_{\text{mal}}^{\text{last}}(n) > c_{\text{SD}}, n = 1, 2, \dots, N\} \\ 0, & \text{others} \end{cases}. \quad (14)$$

To mitigate false positives (FP) and false negatives (FN), we have established the $\frac{W}{4} / \frac{W}{2}$ rule, which considers the number of array elements, to detect anomalous elements. Specifically, when a suspicious abnormal element is detected, the algorithm calculates the sum of d_n over the subsequent $W/2$ elements, denoted as outlier sum (OS). If $\text{OS} \geq W/4$, the element is classified as a reliable abnormal element. This rule is based on the characteristic of the R-MCD, which inherently estimates using only the smallest 75% of anomaly values within the window. Consequently, if elements from the next subarray entering the window exceed $W/4$, they substantially affect the mean and variance estimation. Therefore, if elements entering

the window from the next subarray do not exceed $W/4$, the window's last element is typically flagged as a suspicious abnormal element. Through this method, we effectively reduce the misjudgment rate and enhance the accuracy of anomaly detection.

The detected SnS birth-death points are sorted and expressed as:

$$\hat{\mathcal{C}} = \text{sort}(\mathcal{C}) = \{c_0, c_1, c_2, \dots, c_{N_s-1}, c_{N_s}\}, \quad (15)$$

where $1 = c_0 < c_1 < \dots < c_{N_s} = N + 1$. Here, N_s denotes the number of subarrays obtained from the segmentation. The index set of array elements contained in the n_s -th subarray is given by $\mathcal{P}_{n_s} = \{c_{n_s-1}, c_{n_s-1} + 1, \dots, c_{n_s} - 1\}$. The specific implementation of the above process is illustrated in Fig. 4(a). Furthermore, Fig. 4(b) presents the complete workflow of PASS algorithm.

The computational complexity of the PASS algorithm is mainly from the MCD and the SD computation. For the MCD, when the number of observations increases, its computational complexity decreases sub-linearly. During the sliding window process, the window performs MCD and SD calculations N times, respectively, leading to an overall complexity of approximately $\mathcal{O}(N(1 + \log W))$.

2) *Performance*: This subsection evaluates the performance of the PASS algorithm. The simulation setup is configured as follows: the antenna number is set to $N = 256, 512, 1024$, and the minimum SI is defined at three levels: $\text{SI}_{\min} = 32, 64, 128$. To quantitatively evaluate the accuracy of subarray segmentation, the area under curve (AUC) is employed as the performance metric, with its value ranging from $[0.5, 1]$:

$$\text{AUC} = \int_0^1 \text{REC} * \text{FRP} df. \quad (16)$$

In this context, the recall (REC) is calculated as $\text{REC} = \frac{\text{TP}}{\text{TP} + \text{FN}}$, and the false positive rate (FPR) is calculated as $\text{FPR} = \frac{\text{FP}}{\text{FP} + \text{TN}}$. A higher AUC value in this scenario indicates a stronger ability of the algorithm to distinguish between true SnS birth-death points and false ones, thereby reflecting superior algorithm performance.

As shown in Fig. 5, 1000 Monte Carlo simulations were conducted with power fluctuation variance σ_s^2 set to 5 and 10, and fluctuations confined to $[\underline{t}_s, \bar{t}_s] = [0, 1]$. The results reveal that for a fixed antenna count $N = 512$, the AUC increases as the SI expands, indicating improved algorithm performance as the channel stabilizes. Additionally, as the number of UEs K grows, despite stronger subarray power fluctuations, the AUC remains stable, demonstrating the robustness of the algorithm. Finally, comparing AUC under different σ_s^2 , performance only slightly degrades with higher variance, confirming the algorithm's stability to power fluctuations.

D. DHBF Architecture-Assisted Array Partitioning

The advantages of DHBF architecture in the SnS scenario have been briefly discussed [4]. Therefore, we can similarly adopt this architecture to achieve the decoupling of subarrays. When employing the DHBF architecture, it is recommended to set subarrays with received power below the threshold η_l to an

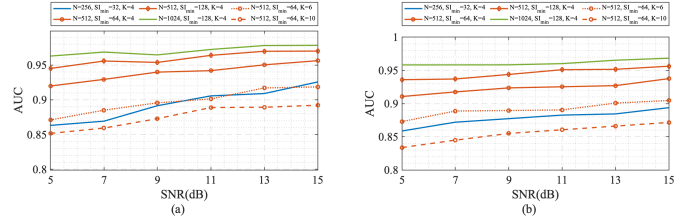


Fig. 5. Impact of SNR on AUC of the PASS algorithm, (a) $\sigma_s^2 = 5$, (b) $\sigma_s^2 = 10$.

off-mode to optimize resource utilization. Let \hat{N}_S denote the number of on-mode subarrays. For simplicity, the distinction between \hat{N}_S and N_S will not be made in the following discussion.

This paper considers an XL-MIMO communication system based on uplink time-division duplex (TDD), where M subcarriers simultaneously serve K single-antenna users. The BS is equipped with a DHBF architecture comprising N_{RF} RF chains and a uniform linear array (ULA) with N antenna elements. Since different users employ orthogonal pilot sequences during the CE phase, an arbitrary user will be considered in the following sections. The received signal at the BS for the m -th subcarrier at the p -th time slot, denoted as $\mathbf{y}_{m,p} \in \mathbb{C}^{N_{\text{RF}} \times 1}$, can be expressed as:

$$\mathbf{y}_{m,p} = \mathbf{U}_p \mathbf{h}_m s_{m,p} + \mathbf{U}_p \mathbf{n}_{m,p}, \quad (17)$$

where $\mathbf{h}_m \in \mathbb{C}^{N \times 1}$ denotes the channel matrix for the m -th subcarrier, $\mathbf{U}_p \in \mathbb{C}^{N_{\text{RF}} \times N}$ represents the combiner matrix at the BS for the p -th time slot, $s_{m,p}$ is the pilot symbol transmitted by the UE at the p -th time slot, and $\mathbf{n}_{m,p} \in \mathbb{C}^{N \times 1}$ is the complex Gaussian noise following $\mathcal{CN}(0, \sigma_{m,p}^2 \mathbf{I}_N)$.

For the DHBF architecture, we reformulate the combiner matrix as:

$$\mathbf{U}_p = [\mathbf{U}_{p,1}^T, \mathbf{U}_{p,2}^T, \dots, \mathbf{U}_{p,N_{\text{RF}}}^T]^T, \quad (18)$$

where $\mathbf{U}_{p,n_{\text{RF}}} \in \mathbb{C}^{1 \times N}$ represents the combiner matrix corresponding to the n_{RF} -th RF chain under a fully-connected architecture. Similarly, $\mathbf{H}_m = [\mathbf{h}_{m,1}^T, \dots, \mathbf{h}_{m,N_{\text{RF}}}^T]^T$ and $\mathbf{n}_{m,p} = [\mathbf{n}_{m,p,1}^T, \dots, \mathbf{n}_{m,p,N_{\text{RF}}}^T]^T$. Since each RF chain is connected to a subset of antenna elements with subarrays as the basic unit, let $\mathcal{S}^{n_{\text{RF}}}$ denote the set of subarray indices connected to the n_{RF} -th RF chain, and $N_S^{n_{\text{RF}}} = |\mathcal{S}^{n_{\text{RF}}}|$ represents the number of connected subarrays. Correspondingly, the set of antenna element indices connected to this RF chain can be denoted as $\mathcal{J}_{n_{\text{RF}}}$, where $N_{n_{\text{RF}}} = |\mathcal{J}_{n_{\text{RF}}}|$ represents the number of antenna elements connected to the n_{RF} -th RF chain. Therefore, the combiner matrix corresponding to the n_{RF} -th RF chain should be expressed as $\mathbf{U}_{p,n_{\text{RF}}} = \mathbf{U}_p(n_{\text{RF}}, \mathcal{J}_{n_{\text{RF}}})^1$. Similarly, we have $\mathbf{h}_{m,n_{\text{RF}}} = \mathbf{h}_m(\mathcal{J}_{n_{\text{RF}}})$ and $\mathbf{n}_{m,p,n_{\text{RF}}} = \mathbf{n}_{m,p}(\mathcal{J}_{n_{\text{RF}}})$.

For the n_{RF} -th RF chain, the received signal at the p -th symbol time on the m -th subcarrier is given by:

$$\mathbf{y}_p^{m,n_{\text{RF}}} = \mathbf{U}_{p,n_{\text{RF}}} \mathbf{h}_{m,n_{\text{RF}}} s_{m,p} + \mathbf{U}_{p,n_{\text{RF}}} \mathbf{n}_{m,p,n_{\text{RF}}}. \quad (19)$$

¹This paper follows the Matlab syntax: Given index sets \mathcal{A} and \mathcal{B} , the expression $\mathbf{v}(\mathcal{A})$ for a vector \mathbf{v} represents extracting elements in the order of \mathcal{A} and forming a new vector; for a matrix \mathbf{M} , the expression $\mathbf{M}(\mathcal{A}, \mathcal{B})$ represents selecting rows based on \mathcal{A} and columns based on \mathcal{B} to reconstruct a new matrix.

The DHBF architecture can control the RF chains to connect to the corresponding array elements autonomously. Considering that N_{RF} is limited in practice, when $N_S \leq N_{\text{RF}}$, a subarray can definitely connect to an RF chain and ensure no coupling between subarrays, i.e., $\{N_S^{n_{\text{RF}}}\}_{n_{\text{RF}}=1}^{N_{\text{RF}}} \leq 1$.

When $N_S > N_{\text{RF}}$, to ensure that all subarrays are connected to the RF chains, multiple subarrays need to share a single RF chain, i.e., $\{N_S^{n_{\text{RF}}}\}_{n_{\text{RF}}=1}^{N_{\text{RF}}} \geq 1$. This configuration inevitably introduces coupling issues between subarrays. In [17], a subarray decoupling method based on GTBC was proposed. However, this method assumes that the subarrays are equally partitioned and relies on the HBF architecture. Consequently, when the SnS birth-death points occur within the predefined subarrays, the accuracy of this algorithm is significantly compromised. Moreover, under the premise of ensuring decoupling accuracy, the pilot length required for CE with GTBC increases linearly with the number of subarrays. To address these issues, we propose an improved algorithm, termed subarray segmentation-based group time block code (SS-GTBC), which enhances the GTBC by integrating the DHBF architecture and leveraging the obtained subarray set $\{\mathcal{P}_1, \dots, \mathcal{P}_{N_s}\}$.

Let $N_S^{n_{\text{RF}}} = 2^j$, where $j \in \mathbb{Z}^+$. Following the GTBC scheme, the combiner matrix encoding is performed as follows:

$$\begin{aligned} & \left[\mathbf{U}_{p, n_{\text{RF}}}^{\text{T}} \quad \mathbf{U}_{p+1, n_{\text{RF}}}^{\text{T}} \quad \dots \quad \mathbf{U}_{p+N_S^{n_{\text{RF}}}-1, n_{\text{RF}}}^{\text{T}} \right]^{\text{T}} \\ &= \begin{bmatrix} \mathbf{U}_{p,1}^{n_{\text{RF}}} & \mathbf{U}_{p,2}^{n_{\text{RF}}} & \dots & \mathbf{U}_{p,N_S^{n_{\text{RF}}}}^{n_{\text{RF}}} \\ \mathbf{U}_{p,1}^{n_{\text{RF}}} & \mathbf{U}_{p,2}^{n_{\text{RF}}} & \dots & \mathbf{U}_{p,N_S^{n_{\text{RF}}}}^{n_{\text{RF}}} \\ \vdots & \vdots & \ddots & \vdots \\ \mathbf{U}_{p,1}^{n_{\text{RF}}} & \mathbf{U}_{p,2}^{n_{\text{RF}}} & \dots & \mathbf{U}_{p,N_S^{n_{\text{RF}}}}^{n_{\text{RF}}} \end{bmatrix} \odot \tilde{\mathfrak{H}}_{N_S^{n_{\text{RF}}}}, \end{aligned} \quad (20)$$

where $\tilde{\mathfrak{H}}_{N_S^{n_{\text{RF}}}}$ is given by (21). In (21), $\mathfrak{H}_{N_S^{n_{\text{RF}}}}^{n_{\text{RF}}}$ denotes the Hadamard matrix of order $N_S^{n_{\text{RF}}}$, and $\mathbf{U}_{p,l}^{n_{\text{RF}}} = \mathbf{U}_{p, n_{\text{RF}}}(\mathcal{S}^{n_{\text{RF}}}\{l\})$, where $\mathcal{S}^{n_{\text{RF}}}\{l\}$ represents the antenna element index set of the l -th subarray connected to the n_{RF} -th RF chain, and $|\mathcal{S}^{n_{\text{RF}}}\{l\}|$ represents the number of antenna elements in that subarray.

Regarding the above encoding process, the decoding for subarray decoupling is expressed as:

$$\begin{bmatrix} \hat{y}_{j,1}^{m, n_{\text{RF}}} \\ \hat{y}_{j,2}^{m, n_{\text{RF}}} \\ \vdots \\ \hat{y}_{j, N_S^{n_{\text{RF}}}}^{m, n_{\text{RF}}} \end{bmatrix} = \frac{1}{N_S^{n_{\text{RF}}}} \mathfrak{H}_{N_S^{n_{\text{RF}}}}^{n_{\text{RF}}} \begin{bmatrix} y_{(j-1) \times N_S^{n_{\text{RF}}} + 1}^{m, n_{\text{RF}}} \\ y_{(j-1) \times N_S^{n_{\text{RF}}} + 2}^{m, n_{\text{RF}}} \\ \vdots \\ y_{j \times N_S^{n_{\text{RF}}}}^{m, n_{\text{RF}}} \end{bmatrix}. \quad (22)$$

If the pilot length is P , then for the n_{RF} -th RF chain, the received signal of the l -th subarray after decoupling is given by $\hat{y}_l^{m, n_{\text{RF}}} = \left[\hat{y}_{1,l}^{m, n_{\text{RF}}}, \hat{y}_{2,l}^{m, n_{\text{RF}}}, \dots, \hat{y}_{P/N_S^{n_{\text{RF}}}, l}^{m, n_{\text{RF}}} \right]^{\text{T}}$.

The previous text briefly outlined the SS-GTBC scheme based on subarray partitioning and a DHBF architecture. It

can be observed that, when P is fixed, for a given RF chain, as $N_S^{n_{\text{RF}}}$ increases, the effective received signals obtained will decrease. Consequently, the effective pilots available for CE vary for the subarrays connected to different RF chains.

According to the above description, it is evident that the allocation of RF chains under a given subarray partition is a combinatorial optimization problem that is difficult to solve optimally in a short time. Since the focus of this paper is on CE, better dynamic RF chain allocation methods remain to be explored in future work. In this paper, we propose a low-complexity RF chain allocation algorithm, termed the Max-Element-First Greedy Allocation Algorithm (MEF-GAA), the process is as follows:

- 1) **Initialization:** Let $\mathcal{C} = \{\mathcal{C}_1, \dots, \mathcal{C}_{N_{\text{RF}}}\}$ be N_{RF} empty classes, where each class \mathcal{C}_i is initially an empty set. Let $\{\mathcal{P}_1, \dots, \mathcal{P}_{N_s}\}$ be N_s subarrays, where each subarray \mathcal{P}_j contains n_j elements, and $n_1 \geq \dots \geq n_{N_s}$.
- 2) **Allocation:** For each subarray \mathcal{P}_j (sorted in descending order of n_j): Assign \mathcal{P}_j to the class \mathcal{C}_k that currently has the fewest elements, i.e., $\mathcal{C}_k = \mathcal{C}_k \cup \mathcal{P}_j$, and update the number of elements in class \mathcal{C}_k : $|\mathcal{C}_k| = |\mathcal{C}_k| + n_j$. Repeat the above steps until all subarrays \mathcal{P}_j have been assigned, and each RF chain \mathcal{C}_i is connected to at least one valid subarray.

This method aims to obtain more effective pilots for subarrays with more elements. In summary, under the DHBF-PSSP, we first employ the PASS algorithm for subarray partitioning, then utilize the MEF-GAA to allocate RF chains. Based on this, we perform subarray decoupling using the SS-GTBC according to the number of subarrays connected to each RF chain, and finally, conduct CE for each subarray using the decoupled effective pilots. In the next section, we will elaborate on our near-field CE methods.

IV. A NEAR-FIELD CHANNEL ESTIMATION METHOD BASED ON THE DFT CODEBOOK

Due to the high storage and computational demands of polar-domain codebooks, as well as the varying apertures of the partitioned subarrays, the corresponding Rayleigh distances differ significantly. Consequently, uniformly applying polar-domain codebooks across all subarrays would inevitably lead to severe computational resource wastage and reduced system efficiency. Studies in [16], [35] have shown that although the angular-domain sparsity of near-field channels is somewhat diminished, the energy leakage remains confined to a limited range. This characteristic ensures that the angular-domain channel exhibits weak sparsity in LoS-dominant mmWave communication systems. Furthermore, [36] highlights that the near-field angular-domain channel exhibits a block-sparse pattern, meaning its support set is distributed in a block-like manner.

Building upon the aforementioned theoretical analysis and integrated with the subarray partitioning scheme, this paper

$$\tilde{\mathfrak{H}}_{N_s}^{n_{\text{RF}}} = \left[\mathfrak{H}_{N_s}^{n_{\text{RF}}}(:, 1) \otimes \mathbf{1}_{1 \times |\mathcal{S}^{n_{\text{RF}}}\{1\}|}, \mathfrak{H}_{N_s}^{n_{\text{RF}}}(:, 2) \otimes \mathbf{1}_{1 \times |\mathcal{S}^{n_{\text{RF}}}\{2\}|}, \dots, \mathfrak{H}_{N_s}^{n_{\text{RF}}}(:, N_S^{n_{\text{RF}}}) \otimes \mathbf{1}_{1 \times |\mathcal{S}^{n_{\text{RF}}}\{N_S^{n_{\text{RF}}}\}|} \right] \quad (21)$$

proposes a CE algorithm that employs DFT codebooks to jointly exploit the angular-domain block sparsity of near-field channels and the inter-subcarrier structured sparsity. Inspired by the diversified sparsity capturing capability of DivSBL in [37], the developed SS-ABSBL-MMV algorithm distinctively incorporates structured sparsity constraints to enhance estimation accuracy and computational efficiency through systematic fusion of near-field channel characteristics.

A. SS-ABSBL-MMV Assisted by Block-Structured Sparsity

For each subarray after decoupling, here is a rephrased version of the effective received signal at the p -th pilot time for the m -th subcarrier:

$$\mathbf{y}_{m,p} = \Phi_p \mathbf{h}_m s_{m,p} + \mathbf{n}_{m,p}, \quad (23)$$

where $\Phi_p \in \mathbb{C}^{N_{\text{RF}} \times N}$ denotes the combiner matrix at the p -th pilot time, \mathbf{h}_m represents the channel matrix under the m -th subcarrier, $s_{m,p}$ is the current pilot symbol. Without loss of generality, it is assumed that $\{s_{m,p}\}_{p=1}^P = 1$, and $\mathbf{n}_{m,p} \in \mathbb{C}^{N_{\text{RF}} \times 1}$ is the additive Gaussian white noise following $\mathcal{CN}(\mathbf{0}, \sigma^2 \mathbf{I})$. Therefore, the received signals at the m -th subcarrier for all P pilot times can be written as:

$$\mathbf{y}_m = \Phi \mathbf{h}_m + \mathbf{n}_m, \quad (24)$$

where $\mathbf{y}_m = [\mathbf{y}_{m,1}^T, \dots, \mathbf{y}_{m,P}^T]^T \in \mathbb{C}^{PN_{\text{RF}} \times 1}$, $\Phi = [\Phi_1^T, \dots, \Phi_P^T]^T \in \mathbb{C}^{PN_{\text{RF}} \times N}$, and $\mathbf{n}_m = [\mathbf{n}_{m,1}^T, \dots, \mathbf{n}_{m,P}^T]^T \in \mathbb{C}^{PN_{\text{RF}} \times 1}$. Then, the received signals across all M subcarriers can be expressed in a more compact form as:

$$\mathbf{Y} = \Phi \mathbf{H} + \mathbf{N}. \quad (25)$$

Among them, $\mathbf{Y} = [\mathbf{y}_1, \dots, \mathbf{y}_M] \in \mathbb{C}^{PN_{\text{RF}} \times M}$, $\mathbf{H} = [\mathbf{h}_1, \dots, \mathbf{h}_M] \in \mathbb{C}^{N \times M}$, and $\mathbf{N} = [\mathbf{n}_1, \dots, \mathbf{n}_M] \in \mathbb{C}^{PN_{\text{RF}} \times M}$. The channel matrix is represented in the angular domain as:

$$\mathbf{Y} = \Psi \mathbf{X} + \mathbf{N}, \quad (26)$$

where $\mathbf{X} = [\mathbf{x}_1, \dots, \mathbf{x}_M] \in \mathbb{C}^{N \times M}$ is the angular-domain channel matrix. Let the sensing matrix $\Psi = \Phi \mathbf{D}$. Here \mathbf{D} is the DFT dictionary matrix.

Assuming that \mathbf{x}_m across subcarriers are independent and follow $\mathcal{CN}(\mathbf{0}, \mathbf{V}_m)$. To accurately capture the unique block sparsity characteristic of the near-field channel in the angular domain, we partition \mathbf{x}_m . Without loss of generality, we assume that \mathbf{x}_m is divided into G blocks of the same length K , and $N = GK$. Therefore, \mathbf{x}_m can be written as:

$$\mathbf{x}_m = \underbrace{[x_{1,1}^m, x_{1,2}^m, \dots, x_{1,K}^m]}_{\text{1-st block } \mathbf{x}_g^m}, \dots, \underbrace{[x_{G,1}^m, \dots, x_{G,K}^m]}_{\text{G-th block } \mathbf{x}_G^m}. \quad (27)$$

To capture the intra-block diversity and inter-block correlation, we model the prior distribution of the g -th block \mathbf{x}_g^m as [37]:

$$p(\mathbf{x}_g^m; \{\mathbf{Q}_g^m, \mathbf{P}_g^m\}) = \mathcal{CN}(\mathbf{0}, \mathbf{Q}_g^m \mathbf{P}_g^m \mathbf{Q}_g^m), \quad (28)$$

where $\mathbf{Q}_g^m = \text{diag}\{\sqrt{\gamma_{g,1}^m}, \dots, \sqrt{\gamma_{g,K}^m}\}$ is used to capture the intra-block variance diversity, and \mathbf{P}_g^m is used to capture

the inter-block variance correlation, which is composed of ℓ_{ij}^m for all $i, j = 1, \dots, K$. By assembling all the blocks, we can obtain $\mathbf{V}_m = \text{diag}\{\mathbf{Q}_1^m \mathbf{P}_1^m \mathbf{Q}_1^m, \dots, \mathbf{Q}_G^m \mathbf{P}_G^m \mathbf{Q}_G^m\}$.

Noting that in multi-carrier systems, the near-field angular-domain channel sparsity exhibits a structured characteristic, i.e., the same block support structure exists under different subcarriers f_m , a feature referred to as BMMV [36]. Therefore, for each block \mathbf{x}_g^m , they share the same covariance matrix across different subcarriers f_m , i.e., $\mathbf{Q}_g^m \mathbf{P}_g^m \mathbf{Q}_g^m = \mathbf{Q}_g \mathbf{P}_g \mathbf{Q}_g$ ($\forall m$).

To elucidate the BMMV problem, the original problem is reformulated as:

$$\tilde{\mathbf{y}} = \tilde{\Psi} \tilde{\mathbf{x}} + \tilde{\mathbf{n}}. \quad (29)$$

Among them, $\tilde{\mathbf{y}} = \text{vec}(\mathbf{Y}^T) \in \mathbb{C}^{PMN_{\text{RF}} \times 1}$, $\tilde{\Psi} = \Psi \otimes \mathbf{I}_M \in \mathbb{C}^{PMN_{\text{RF}} \times MN}$, $\tilde{\mathbf{x}} = \text{vec}(\mathbf{X}^T) \in \mathbb{C}^{MN \times 1}$, and $\tilde{\mathbf{n}} = \text{vec}(\mathbf{N}^T) \in \mathbb{C}^{PMN_{\text{RF}} \times 1}$. Then, for the reconstructed $\tilde{\mathbf{x}}$, it can still be divided into G blocks, with the channel vector in each block being $\tilde{\mathbf{x}}_g = [x_{g,1}^1, \dots, x_{g,K}^1, \dots, x_{g,1}^M, \dots, x_{g,K}^M]^T \in \mathbb{C}^{MK \times 1}$, then we have:

$$p(\tilde{\mathbf{x}}_g; \{\mathbf{Q}_g, \mathbf{P}_g\}) = \mathcal{CN}(\mathbf{0}, \mathbf{I}_M \otimes \mathbf{Q}_g \mathbf{P}_g \mathbf{Q}_g). \quad (30)$$

By assembling all the blocks, the prior distribution of $\tilde{\mathbf{x}}$ is following $\mathcal{CN}(\mathbf{0}, \tilde{\mathbf{V}})$, where $\tilde{\mathbf{V}} = \text{diag}\{\mathbf{I}_M \otimes \mathbf{Q}_1 \mathbf{P}_1 \mathbf{Q}_1, \dots, \mathbf{I}_M \otimes \mathbf{Q}_G \mathbf{P}_G \mathbf{Q}_G\}$.

Based on the observation of $\tilde{\mathbf{y}}$, the Gaussian likelihood function can be obtained as:

$$p(\tilde{\mathbf{y}} | \tilde{\mathbf{x}}, \sigma^2) = \mathcal{CN}(\tilde{\Psi} \tilde{\mathbf{x}}, \sigma^2 \mathbf{I}). \quad (31)$$

Leveraging the Bayesian estimation principle and the properties of the multivariate Gaussian distribution, the posterior probability distribution can be derived as:

$$p(\tilde{\mathbf{x}} | \tilde{\mathbf{y}}; \{\mathbf{Q}_g, \mathbf{P}_g\}_{g=1}^G, \sigma^2) = \mathcal{CN}(\boldsymbol{\mu}_x, \boldsymbol{\Sigma}_x), \quad (32)$$

where

$$\begin{aligned} \boldsymbol{\mu}_x &= \tilde{\mathbf{V}} \tilde{\Psi}^H \left(\sigma^2 \mathbf{I} + \tilde{\Psi} \tilde{\mathbf{V}} \tilde{\Psi}^H \right)^{-1} \tilde{\mathbf{y}}, \\ \boldsymbol{\Sigma}_x &= \tilde{\mathbf{V}} - \tilde{\mathbf{V}} \tilde{\Psi}^H \left(\sigma^2 \mathbf{I} + \tilde{\Psi} \tilde{\mathbf{V}} \tilde{\Psi}^H \right)^{-1} \tilde{\Psi} \tilde{\mathbf{V}}. \end{aligned} \quad (33)$$

By estimating the hyperparameters $\Theta = \{\{\mathbf{Q}_g, \mathbf{P}_g\}_{g=1}^G, \sigma^2\}$, the MAP estimate of $\tilde{\mathbf{x}}$ can be obtained as $\hat{\boldsymbol{\mu}} = \boldsymbol{\mu}_x$.

Next, the Expectation-Maximization (EM) algorithm is employed to estimate the hyperparameters Θ . The main idea of estimating Θ using the EM algorithm is to maximize the likelihood function $p(\tilde{\mathbf{y}} | \tilde{\mathbf{x}}, \Theta)$, which is equivalent to:

$$\min_{\Theta} \mathcal{L}(\Theta) = -\ln p(\tilde{\mathbf{y}} | \tilde{\mathbf{x}}, \Theta) = \tilde{\mathbf{y}}^H \boldsymbol{\Sigma}_y^{-1} \tilde{\mathbf{y}} + \ln |\boldsymbol{\Sigma}_y|, \quad (34)$$

where $\boldsymbol{\Sigma}_y = \sigma^2 \mathbf{I} + \tilde{\Psi} \tilde{\mathbf{V}} \tilde{\Psi}^H$. In the E-step, $\tilde{\mathbf{x}}$ is treated as a latent variable, and the following Q -function is maximized:

$$\begin{aligned} Q(\Theta) &= \mathbb{E}_{\tilde{\mathbf{x}} | \tilde{\mathbf{y}}, \Theta^{(t-1)}} [p(\tilde{\mathbf{y}}, \tilde{\mathbf{x}}; \Theta)] \\ &= \mathbb{E}_{\tilde{\mathbf{x}} | \tilde{\mathbf{y}}, \Theta^{(t-1)}} [p(\tilde{\mathbf{y}} | \tilde{\mathbf{x}}, \sigma^2)] \\ &\quad + \mathbb{E}_{\tilde{\mathbf{x}} | \tilde{\mathbf{y}}, \Theta^{(t-1)}} [p(\tilde{\mathbf{x}}, \{\mathbf{Q}_g, \mathbf{P}_g\}_{g=1}^G)]. \end{aligned} \quad (35)$$

The aforementioned Q -function is divided into parts that solely contain the hyperparameter σ^2 and those that solely contain the hyperparameters $\{\mathbf{Q}_g, \mathbf{P}_g\}_{g=1}^G$. In the M-step, we obtain estimates of Θ by maximizing the $Q(\Theta)$. First, focusing on the term $\mathbb{E}_{\tilde{\mathbf{x}}|\tilde{\mathbf{y}}, \Theta^{(t-1)}} [p(\tilde{\mathbf{x}}, \{\mathbf{Q}_g, \mathbf{P}_g\}_{g=1}^G)]$, it can be expressed as:

$$\begin{aligned} & \mathbb{E}_{\tilde{\mathbf{x}}|\tilde{\mathbf{y}}, \Theta^{(t-1)}} [p(\tilde{\mathbf{x}}, \{\mathbf{Q}_g, \mathbf{P}_g\}_{g=1}^G)] \\ & \propto -\frac{1}{2} \ln |\tilde{\mathbf{V}}| - \frac{1}{2} \text{tr} [\tilde{\mathbf{V}}^{-1} (\boldsymbol{\Sigma}_{\mathbf{x}} + \boldsymbol{\mu}_{\mathbf{x}} \boldsymbol{\mu}_{\mathbf{x}}^H)]. \end{aligned} \quad (36)$$

Estimating \mathbf{Q}_g is equivalent to estimating $\{\sqrt{\gamma_{g,k}}\}_{k=1}^K$. Therefore, to maximize (36), we first take the derivative of its first part:

$$\frac{\partial (-\frac{1}{2} \ln |\mathbf{V}|)}{\partial \sqrt{\gamma_{g,k}}} = \frac{\partial (-\frac{M}{2} \sum_{i=1}^G |\mathbf{Q}_i \mathbf{P}_i \mathbf{Q}_i|)}{\partial \sqrt{\gamma_{g,k}}} = \frac{-M}{\sqrt{\gamma_{g,k}}}. \quad (37)$$

Then take the derivative of the second term:

$$\begin{aligned} & \frac{\partial \left(-\frac{1}{2} \text{tr} [\tilde{\mathbf{V}}^{-1} (\boldsymbol{\Sigma}_{\mathbf{x}} + \boldsymbol{\mu}_{\mathbf{x}} \boldsymbol{\mu}_{\mathbf{x}}^H)] \right)}{\partial \sqrt{\gamma_{g,k}}} \\ & = \gamma_{g,k}^{-\frac{3}{2}} (\mathbf{P}_g^{-1})_{k,k} \sum_{m=1}^M (\mathbf{R}^g)_{mk,mk} \\ & + \gamma_{g,k}^{-1} \left[(\mathbf{P}_g^{-1})_{k,\cdot} \odot \mathbf{W}_{g \setminus k}^{-1} \right] \sum_{m=1}^M (\mathbf{R}^g)_{\cdot,mk}, \end{aligned} \quad (38)$$

where $\mathbf{R}^g = (\boldsymbol{\Sigma}_{\mathbf{x}}^g + \boldsymbol{\mu}_{\mathbf{x}}^g \boldsymbol{\mu}_{\mathbf{x}}^{gH})$, $\boldsymbol{\mu}_{\mathbf{x}}^g = \boldsymbol{\mu}_{\mathbf{x}}((g-1)MK + 1 : gMK)$ and $\boldsymbol{\Sigma}_{\mathbf{x}}^g = ((g-1)MK + 1 : gMK, (g-1)MK + 1 : gMK)$, while $(\cdot)_{i,j}$ denotes the element at the (i,j) -th index of the matrix. Additionally, $\mathbf{W}_{g \setminus k} = \text{diag} \{ \sqrt{\gamma_{g,1}}, \dots, \sqrt{\gamma_{g,k-1}}, 0, \sqrt{\gamma_{g,k+1}}, \dots, \sqrt{\gamma_{g,K}} \}$.

By combining the above derivative expressions and setting them to zero, we obtain:

$$\gamma_{g,k} = \frac{4\mathbf{A}_{g,k}^2}{\left(\sqrt{\mathbf{B}_{g,k}^2} + 4M\mathbf{A}_{g,k} - \mathbf{B}_{g,k} \right)^2}. \quad (39)$$

In the above equation,

$$\begin{aligned} \mathbf{A}_{g,k} &= (\mathbf{P}_g^{-1})_{k,k} \sum_{m=1}^M (\mathbf{R}^g)_{mk,mk}, \\ \mathbf{B}_{g,k} &= \left[(\mathbf{P}_g^{-1})_{k,\cdot} \odot \text{diag} (\mathbf{W}_{g \setminus k}^{-1}) \right] \sum_{m=1}^M (\mathbf{R}^g)_{\cdot,mk}. \end{aligned}$$

Similarly, by taking the derivative of both parts of (36) with respect to \mathbf{P}_g , we obtain:

$$\begin{aligned} & \frac{\partial \left(-\frac{1}{2} \ln |\tilde{\mathbf{V}}| - \frac{1}{2} \text{tr} [\tilde{\mathbf{V}}^{-1} (\boldsymbol{\Sigma}_{\mathbf{x}} + \boldsymbol{\mu}_{\mathbf{x}} \boldsymbol{\mu}_{\mathbf{x}}^H)] \right)}{\partial \mathbf{P}_g} \\ & = -\frac{M}{2} \mathbf{P}_g^{-1} + \frac{1}{2} \sum_{m=1}^M [\mathbf{P}_g^{-1} \mathbf{Q}_g^{-1} (\mathbf{R}^g)_m \mathbf{Q}_g^{-1} \mathbf{P}_g^{-1}], \end{aligned} \quad (40)$$

where $(\mathbf{R}^g)_m = \mathbf{R}^g((m-1)K + 1 : mK, (m-1)K + 1 : mK)$. Combine the above derivation and set it to zero to get:

$$\mathbf{P}_g = \frac{1}{M} \mathbf{Q}_g^{-1} \sum_{m=1}^M (\mathbf{R}^g)_m \mathbf{Q}_g^{-1}. \quad (41)$$

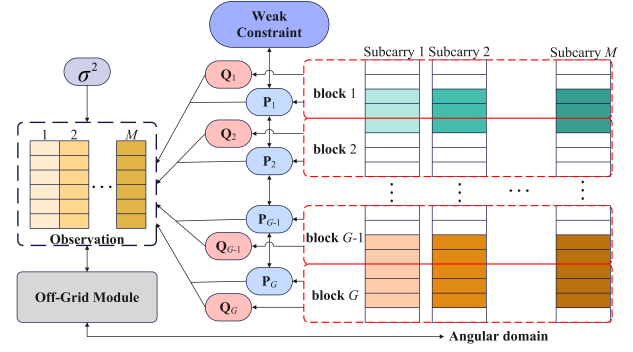


Fig. 6. Diagram of ABSBL using MMV framework and Off-grid module.

The likelihood function for σ^2 is derived in a similar manner. Take the derivative of it and set the derivative to zero to get:

$$\sigma_{(t)}^2 = \frac{\|\tilde{\mathbf{y}} - \tilde{\mathbf{\Psi}} \boldsymbol{\mu}_{\mathbf{x}}\|_2^2 + \sigma_{(t-1)}^2 [NM - \text{tr} (\boldsymbol{\Sigma}_{\mathbf{x}} \tilde{\mathbf{V}}^{-1})]}{MPN_{\text{RF}}}. \quad (42)$$

To prevent overfitting of \mathbf{P}_g to the data while ensuring diversity in inter-block variance, the \mathbf{P}_g should be corrected by imposing constraints. Specifically, the unconstrained maximization of $\mathbb{E}_{\tilde{\mathbf{x}}|\tilde{\mathbf{y}}, \Theta^{(t-1)}} [p(\tilde{\mathbf{x}}, \{\mathbf{Q}_g, \mathbf{P}_g\}_{g=1}^G)]$ is transformed into a constrained maximization. This paper adopts the weak constraint function $\ln[\det(\cdot)]$, and thus the original problem becomes [37]:

$$\begin{aligned} \max_{\mathbf{P}_g} & -\frac{1}{2} \ln [\det (\tilde{\mathbf{V}})] - \frac{1}{2} \text{tr} [\tilde{\mathbf{V}}^{-1} (\boldsymbol{\Sigma}_{\mathbf{x}} + \boldsymbol{\mu}_{\mathbf{x}} \boldsymbol{\mu}_{\mathbf{x}}^H)], \\ \text{s.t.} & \ln [\det (\mathbf{I}_M \otimes \mathbf{P}_g)] = \ln [\det (\bar{\mathbf{P}})] \end{aligned} \quad (43)$$

where $\bar{\mathbf{P}} = \frac{1}{G} \sum_{g=1}^G (\mathbf{I}_M \otimes \mathbf{P}_g)$.

To solve the aforementioned optimization problem, the augmented Lagrangian method (ALM) can be employed. This involves constructing and minimizing an augmented Lagrangian function $\mathcal{L}(\mathbf{P}_g, \lambda, c)$, where λ is the Lagrange multiplier, and c is the quadratic penalty factor. By solving $\nabla_{\mathbf{P}_g} \mathcal{L}(\mathbf{P}_g, \lambda, c) = 0$ and $\nabla_{\lambda} \mathcal{L}(\mathbf{P}_g, \lambda, c) = 0$, the iterative formulas for the ALM can be obtained as follows:

$$\begin{aligned} \mathbf{P}_g^{(t)} &= \frac{\mathbf{Q}_g^{-1} \sum_{m=1}^M (\mathbf{R}^g)_m \mathbf{Q}_g^{-1}}{M \left[1 + 2\lambda_g^{(t-1)} + 2c \left(M \ln |\mathbf{P}_g^{(t-1)}| - \ln |\bar{\mathbf{P}}^{(t-1)}| \right) \right]}, \\ \lambda_g^{(t)} &= \lambda_g^{(t-1)} + \alpha^{t-1} \left(M \ln |\mathbf{P}_g^{(t-1)}| - \ln |\bar{\mathbf{P}}^{(t-1)}| \right) \end{aligned} \quad (44)$$

where α is the iteration step size of the ALM, and λ_g represents the multiplier associated with the g -th block.

Due to the introduction of the strongly convex term in ALM, its convergence speed is significantly improved compared to the dual ascent method. Additionally, unlike the penalty function method, it does not excessively rely on the magnitude of the penalty parameter, thereby ensuring the numerical accuracy of the solution.

B. Introduction of the Off-Grid Module

The accuracy of angular sparsity-based CE algorithms is constrained by finite discrete grids. Specifically, the DFT codebook used in on-grid angular domain algorithms samples $\sin(\theta_n)$ from $\frac{2n-N-1}{N}, n = 1, \dots, N$. This results in a mismatch between the virtual angles and the true angles. Such mismatch is particularly evident in near-field channels, as it not only causes bias in the target angle estimation but also leads to cascading estimation errors in the corresponding angular spread. To address this issue, we seek a set of angles $\hat{\Xi} = [\hat{\theta}_1, \dots, \hat{\theta}_N]$ and reconstruct the codebook $\mathbf{D}(\hat{\Xi}) = [\mathbf{a}(\hat{\theta}_1), \dots, \mathbf{a}(\hat{\theta}_N)]$ for channel matrix estimation. For a single subcarrier, the optimization problem is:

$$\mathbf{z}^*, \mathbf{x}^* = \arg \min_{\mathbf{z}, \mathbf{x}} \|\mathbf{y} - \Phi \mathbf{D}(\arcsin(\mathbf{z})) \mathbf{x}\|^2, \quad (45)$$

where $\mathbf{z} = \sin \Xi$.

To address the previously mentioned optimization problem, an alternating framework can be employed. Specifically, in each iteration, the sparse coefficient vector is updated first using the least squares (LS) solution:

$$\mathbf{x}^{(t+1)} = \left[\left(\Phi \mathbf{D}^{(t)} \right)^H \Phi \mathbf{D}^{(t)} \right]^{-1} \left(\Phi \mathbf{D}^{(t)} \right)^H \mathbf{y}. \quad (46)$$

For the angular grid, the gradient descent method (GD) is employed for updates, with the following computed first:

$$\nabla_{\mathbf{z}} f^{(t+1)}(\mathbf{z}, \mathbf{x}) = \Re \left[j \frac{2\pi d}{\lambda} \left(\mathbf{y} - \Phi \mathbf{D}^{(t)} \mathbf{x}^{(t+1)} \right)^H \times \text{diag}(0, \dots, N-1) \mathbf{D}^{(t)} \right]. \quad (47)$$

Simultaneously, the update step size of the GD is determined by the backtracking line search approach, and the iterative formula is obtained:

$$\mathbf{z}^{(t+1)} = \mathbf{z}^{(t)} - \rho^{(t)} \nabla_{\mathbf{z}} f^{(t+1)}(\mathbf{z}, \mathbf{x}), \quad (48)$$

where ρ represents the update step size of GD.

The codebook is updated via $\mathbf{D}^{(t+1)} = \mathbf{D}(\arcsin(\mathbf{z}^{(t+1)}))$. The finally estimated channel matrix is generated by $\mathbf{D}^{(T)} \mathbf{x}^{(T)}$. We refer to the SS-ABSBL-MMV algorithm with an off-grid module as SS-OG-ABSBL-MMV. The schematic diagram of this algorithm is shown in Fig. 6, and the pseudocode is given by Algorithm 1.

C. Computational Complexity

To analyze the computational complexity of various algorithms, the number of antennas at the BS is uniformly set to $N = GK$, and the SnS effect is not considered. For the ABSBL-MMV algorithm, it is assumed that the number of iterations of the ALM is I (typically $I < 10$). During the solution process, the properties of block diagonal matrices are utilized to simplify the calculations. It should be noted that after each iteration of the ABSBL-MMV algorithm, blocks with estimated values below the threshold are directly set to zero and no longer participate in subsequent iterations, where T_{ite} represents the number of iterations of the ABSBL algorithm. Additionally, R_{ite} represents the number of iterations of the off-grid module. In summary, the complexities of the various algorithms are summarized in Table I.

TABLE I
COMPUTATIONAL COMPLEXITY OF ALGORITHMS.

Algorithm	Computational Complexity
ABSBL	$T_{ite}M(NP^2N_{RF}^2 + GK^3 + GK^2 + GIK^3 + NK^2G)$
ABSBL-MMV	$T_{ite}(NM^3P^2N_{RF}^2 + GK^3 + GK^2M + GIK^3 + NM^2K^2G)$
OG-ABSBL	$T_{ite}M(NP^2N_{RF}^2 + GK^3 + GK^2 + GIK^3 + NK^2G) + R_{ite}(P^2N_{RF}^2M + PN_{RF}M^2)$
OG-ABSBL-MMV	$T_{ite}(NM^3P^2N_{RF}^2 + GK^3 + GK^2M + GIK^3 + NM^2K^2G) + R_{ite}(P^2N_{RF}^2M + PN_{RF}M^2)$

V. SIMULATION RESULTS

In this section, we assess the performance of the proposed algorithm under various system settings. We use the normalized mean square error (NMSE) as the metric:

$$\text{NMSE} = \mathbb{E} \left[\frac{\|\hat{\mathbf{H}} - \mathbf{H}\|_F^2}{\|\mathbf{H}\|_F^2} \right]. \quad (49)$$

Algorithm 1 ABSBL Algorithm.

Input: Received signal $\mathbf{Y} \in \mathbb{C}^{PN_{RF} \times M}$; Sensing matrix $\Psi = \Phi \mathbf{D} \in \mathbb{C}^{PN_{RF} \times N}$; Block size $K = N/G$; ABSBL and off-grid module maximum iteration number T_{ite} , R_{ite} , and their corresponding stopping thresholds δ_1 , δ_2 .

Output: Estimated channel matrix $\hat{\mathbf{H}}$.

- 1: **Initialization:** Rearrange \mathbf{Y} and Ψ to $\tilde{\mathbf{y}}$ and $\tilde{\Psi}$ by (29); Set $\mathbf{Q}_g, \mathbf{P}_g = \mathbf{I}_K, \forall g$; Initial noise variance $\sigma_{(0)}^2 = \text{var}(\tilde{\mathbf{y}}) \times 10^{-2}$; Initial multiplier $\lambda_g^{(0)} = 0, \forall g$; Available block index set $\mathcal{L} = \{g\}_{g=1}^G$
 - 2: **% ABSBL Core %**
 - 3: **for** $t = 1 : T_{ite}$ **do**
 - 4: **for** $l \in \mathcal{L}$ **do**
 - 5: **if** $\text{mean}(\text{diag}(\mathbf{Q}_i)) < \text{threshold}$ **then**
 - 6: $\mathcal{L} = \mathcal{L} \setminus \{l\}$; Set $\boldsymbol{\mu}_{\mathbf{x}}^l = \mathbf{0}, \boldsymbol{\Sigma}_{\mathbf{x}}^l = \mathbf{0}_{KM \times KM}$;
 - 7: **end if**
 - 8: Update $\gamma_{l,k}, \forall k$ by (39);
 - 9: Update $\tilde{\mathbf{P}}$ by (41) and (43);
 - 10: Use ALM to update \mathbf{P}_l and λ_l by (44);
 - 11: **end for**
 - 12: Update $\boldsymbol{\mu}_{\mathbf{x}}$ and $\boldsymbol{\Sigma}_{\mathbf{x}}$ by (33);
 - 13: Update σ^2 by (42);
 - 14: **if** $\|\boldsymbol{\mu}_{\mathbf{x}}^{(r+1)} - \boldsymbol{\mu}_{\mathbf{x}}^{(r)}\|^2 < \delta_1$ **then break**;
 - 15: **end for**
 - 16: **% Off-grid Module %**
 - 17: **for** $r = 1 : R_{ite}$ **do**
 - 18: Update $\mathbf{x}^{(r+1)}$ by (46);
 - 19: Compute $\nabla_{\mathbf{z}} f^{(r+1)}$ by (47);
 - 20: Update \mathbf{z}^{r+1} by (48);
 - 21: **if** $\|\mathbf{x}^{(r+1)} - \mathbf{x}^{(r)}\|^2 < \delta_2$ **then break**;
 - 22: **end for**
 - 23: Rearrange to obtain $\hat{\mathbf{H}}$.
-

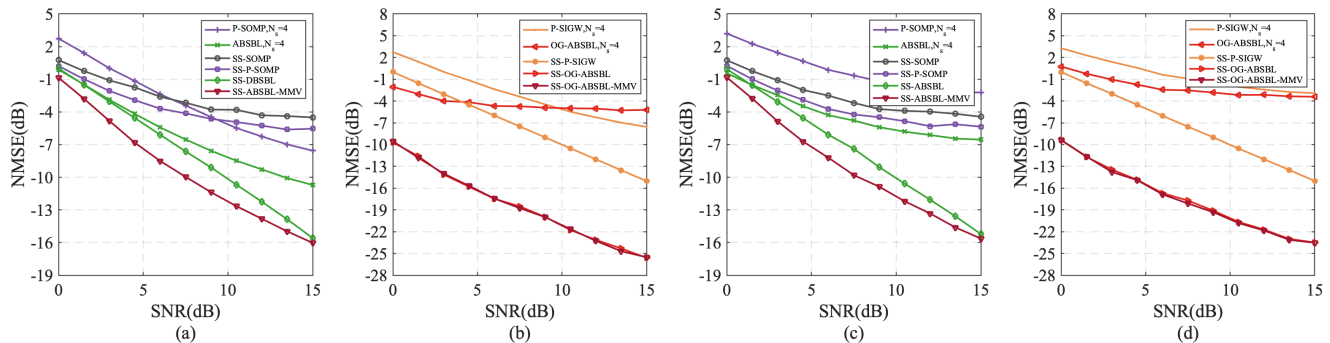


Fig. 7. NMSE versus SNR (a) $P = 64$, On-grid, (b) $P = 64$, Off-grid, (c) $P = 32$, On-grid, (d) $P = 32$, Off-grid.

A. Parameter Configuration

In this simulation, unless otherwise specified, we consider a multi-user LoS XL-MIMO OFDM system. The BS is equipped with $N = 512$ antenna elements and $N_{\text{RF}} = 4$ RF chains, operating at a central frequency of $f_c = 50$ GHz with a system bandwidth of $B = 100$ MHz. A total of $M = 5$ subcarriers are simultaneously used to serve $K = 4$ UEs. The distances and angles of the UEs are sampled from $\mathcal{U}(10\text{m}, 300\text{m})$ and $\mathcal{U}(-2\pi/3, 2\pi/3)$, respectively. The channels used in this simulation are generated by extending the code provided in [17]. We perform 1000 Monte Carlo simulations for statistical validation.

B. Algorithm Description

To evaluate CE performance, some baselines and our proposed method are summarized below.

- **P-SOMP/P-SIGW** [17]: Using an equal subarray partitioning strategy, the on-grid and the off-grid SOMP based on the polar domain codebook are implemented. The number of distance samples in the polar domain codebook is set to 4, and the number of subarrays is set to $N_s = 4$.
- **ABSL/OG-ABSL**: Using an equal subarray partitioning strategy, the on-grid and the off-grid ABSL based on the DFT codebook are implemented. The number of subarrays is set to $N_s = 4$.
- **SS-SOMP** [38]: The on-grid SOMP uses the DFT codebook, based on the PASS proposed in this paper for subarray partitioning.
- **SS-P-SOMP/P-SIGW**: The on-grid and the off-grid SOMP use the polar domain codebook, based on the PASS proposed in this paper for subarray partitioning.
- **SS-ABSL/SS-OG-ABSL**: The on-grid and the off-grid ABSL use the DFT codebook, based on the PASS proposed in this paper for subarray partitioning.
- **SS-ABSL-MMV/SS-OG-ABSL-MMV**: Based on the proposed PASS for subarray partitioning, and leveraging the structured block sparsity among carriers in MMV framework, the on-grid and the off-grid ABSL use the DFT codebook.

C. Impact of SNR

To ensure the fairness of the simulations, we compared the on-grid and off-grid algorithms separately. For the on-grid

architecture, as shown in Fig. 7(a)(c), we compared NMSE of the P-SOMP and ABSL under equal subarray partitioning. The results demonstrate that the proposed ABSL algorithm outperforms the P-SOMP algorithm even under the equal subarray partitioning strategy.

We further applied the proposed DHBF-PSSP to the baseline algorithms. The results showed that the performance of both P-SIGW and ABSL algorithms improved with the aid of DHBF-PSSP, and this improvement became more significant at higher SNR levels. However, the P-SOMP algorithm under the DHBF-PSSP did not improve and even degraded, probably because the precise subarray partitioning in the DHBF-PSSP did not increase the effective pilots for each subarray uniformly. This led to performance loss for the pilot-sensitive P-SOMP algorithm.

Comparing the NMSE of SS-SOMP and SS-P-SOMP algorithms, we found little difference. This is because, in the LoS XL-MIMO system, although angular energy leakage occurs, the sparsity is not completely lost due to the large number of array elements. In contrast, the SS-ABSL algorithm, despite not using a high-complexity polar codebook, outperformed other algorithms, demonstrating both low complexity and high reliability. Moreover, in the MMV framework, the algorithms fully exploited the structured sparsity among subcarriers, resulting in excellent performance at low SNR levels.

For the off-grid architecture, as shown in Fig. 7(b)(d), the results showed that all algorithms except the SS-OG-ABSL algorithm achieved significant performance improvements. The use of the MMV framework had little impact on performance in the off-grid scenario. The performance loss of the SS-OG-ABSL algorithm was mainly due to non-ideal subarray partitioning, which led to interpolation in the angular domain and weakened sparsity. This prevented the ABSL algorithm from accurately identifying the support set. Consequently, the reconstructed codebook in the off-grid module could not correctly restore the channel matrix, leading to performance degradation.

D. Impact of Pilot Length and Beamforming Architecture

To verify the advantage of the DHBF-PSSP architecture in reducing pilot overhead for CE, we applied both the fully-connected HBF-PASS and DHBF-PASS architectures to four

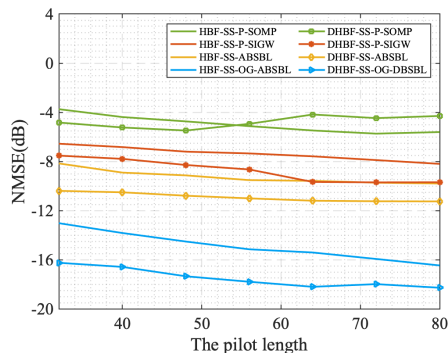


Fig. 8. NMSE versus pilot length and beam-forming architecture.

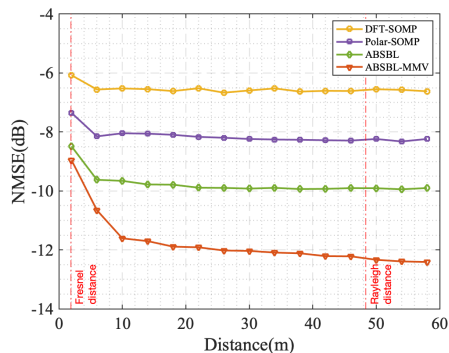


Fig. 9. NMSE versus UE-BS distance.

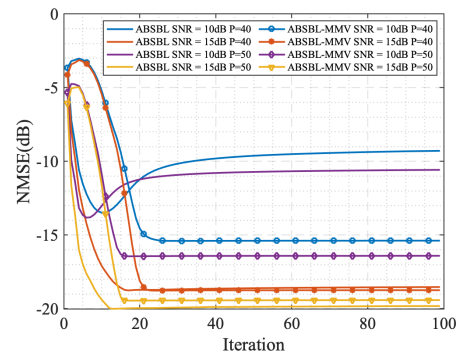


Fig. 10. The convergence of ABSBL.

algorithms: P-SOMP, P-SIGW, ABSBL, and OG-ABSBL. The SNR is set at 10 dB.

The results, as shown in Fig. 8, indicate that even with the DHBF-PSSP architecture using the locally optimal MEF-GAA algorithm, the performance of all CE algorithms was significantly improved under the same pilot length. Specifically, with a fixed number of pilots and known subarray partitioning, the DHBF architecture using the MEF-GAA algorithm effectively increased the number of decoupled effective pilots allocated to each subarray. This finding confirms the superiority of the DHBF-PSSP architecture in optimizing pilot allocation and improving CE accuracy.

E. Impact of Distance

When the near-field spatial channel matrix is transformed into angular domain using the DFT codebook, as the distance between the BS and UE decreases, energy leakage in the angular domain increases significantly, reducing the sparsity of the angular domain. This reduction in sparsity directly impacts the performance of CE algorithms based on CS techniques. To evaluate the performance of the proposed algorithm under varying sparsity conditions, this simulation focuses solely on the discussion of the impact of UE-BS distance on the angular domain sparsity, disregarding the influence of SnS.

The simulation setup employs a fully connected HBF architecture with $N = 128$ BS antennas and $N_{RF} = 4$ RF chains. The pilot length and SNR are set to $P = 20$ and 10 dB. The UE-BS distance gradually increases from 2 m to 58 m. In this system, the Fresnel distance is $R_f = 0.62\sqrt{\frac{D^3}{\lambda}} \approx 1.88$ m, and the Rayleigh distance is $R_r = \frac{2D^2}{\lambda} \approx 48.38$ m. The distance range set in the simulation covers both the near-field and far-field regions.

As depicted in Fig. 9, the performance of all algorithms decreases when the UE-BS distance is less than 10 meters. This decline is attributed to the loss of sparsity due to angular spreading for DFT-based methods and insufficient resolution for P-SOMP due to fewer distance samples. Our proposed ABSBL and ABSBL-MMV algorithms consistently outperform others across different distances.

Notably, algorithm performance stabilizes at around 10 meters, which is much less than the conventional Rayleigh

distance that separates far-field from near-field conditions. This suggests that the Rayleigh distance may overestimate the negative effects of near-field on CE. Based on this fact, existing studies have introduced the concept of the effective Rayleigh distance to more accurately define the strong and weak near-field channels [35], [39].

F. Convergence

To assess the convergence performance of the proposed ABSBL and ABSBL-MMV algorithms, we conducted systematic simulations with the following setup: $N = 256$, $N_{RF} = 4$, and the pilot length was set to $P = 40$ and $P = 50$. The SNR was set at two levels, 10 dB and 15 dB. For each parameter combination, we performed 100 iterations to observe the change in NMSE over iterations.

As shown in Fig. 10, the following conclusions can be drawn. First, across all tested configurations, NMSE decreased with increasing iterations, indicating good convergence. Second, at low SNR (10 dB), the ABSBL showed a characteristic convergence curve that initially decreased, then increased, and finally stabilized, which was not observed at high SNR (15 dB). Notably, the ABSBL-MMV, which leverages inter-carrier structured sparsity, demonstrated significant performance advantages in low SNR environments, with faster convergence than the ABSBL.

Comparing results across different parameter settings, we found that SNR has a more significant impact on algorithm performance than pilot length. Moreover, Fig. 10 provides an important reference for determining the number of iterations needed for CE. Based on the analysis, setting the number of iterations to 30 achieves accurate and stable CE under the simulation conditions of this study.

VI. CONCLUSION

This paper explored the subarray-based near-field channel estimation problem under SnS effects. We first extended the original near-field channel model to accommodate SnS characteristics in LoS XL-MIMO systems. Given that existing SnS near-field channel estimation algorithms assumed equal array partitioning, we theoretically analyzed the limitations of non-ideal subarray configurations. To address this, we proposed a DHBF-PSSP architecture, which included a PASS

algorithm for measurement-driven array partitioning, an SS-GTBC method for subarray decoupling via DHBFB, and an MEF-GAA for RF chain resource allocation under limited RF chain constraints. By using the subarray segmentation, we developed both on-grid and off-grid versions of the SS-ABSBL-MMV algorithm that employed the block sparsity in angular-domain channels and structured sparsity across sub-carriers, thereby reducing computational and storage overhead. Simulation results demonstrated that the proposed framework achieved superior NMSE performance in SnS near-field channel estimation through DHBFB-PSSP. Future work may explore optimal subarray partitioning strategies, enhanced RF chain allocation schemes, and efficient near-field CE algorithms.

REFERENCES

- [1] A. Fayad, T. Cinkler, and J. Rak, "Toward 6G optical fronthaul: A survey on enabling technologies and research perspectives," *IEEE Commun. Surveys Tuts.*, vol. 27, no. 1, pp. 629–666, 2025.
- [2] H. Lu, Y. Zeng, C. You, Y. Han, J. Zhang *et al.*, "A tutorial on near-field XL-MIMO communications toward 6G," *IEEE Commun. Surveys Tuts.*, vol. 26, no. 4, pp. 2213–2257, 2024.
- [3] Z. Wang, J. Zhang, H. Du, D. Niyato, S. Cui *et al.*, "A tutorial on extremely large-scale MIMO for 6G: Fundamentals, signal processing, and applications," *IEEE Commun. Surveys Tuts.*, vol. 26, no. 3, pp. 1560–1605, 2024.
- [4] E. D. Carvalho, A. Ali, A. Amiri, M. Angjelichinoski, and R. W. Heath, "Non-stationarities in extra-large-scale massive MIMO," *IEEE Wireless Commun.*, vol. 27, no. 4, pp. 74–80, 2020.
- [5] J. Flordelis, X. Li, O. Edfors, and F. Tufvesson, "Massive MIMO extensions to the COST 2100 channel model: Modeling and validation," *IEEE Trans. Wireless Commun.*, vol. 19, no. 1, pp. 380–394, 2020.
- [6] J. Lee, G.-T. Gil, and Y. H. Lee, "Channel estimation via orthogonal matching pursuit for hybrid MIMO systems in millimeter wave communications," *IEEE Trans. Commun.*, vol. 64, no. 6, pp. 2370–2386, 2016.
- [7] S. Srivastava, A. Mishra, A. Rajorija, A. K. Jagannatham, and G. Ascheid, "Quasi-static and time-selective channel estimation for block-sparse millimeter wave hybrid MIMO systems: Sparse bayesian learning (SBL) based approaches," *IEEE Trans. Signal Process.*, vol. 67, no. 5, pp. 1251–1266, 2019.
- [8] X. Cheng, J. Sun, and S. Li, "Channel estimation for FDD multi-user massive MIMO: A variational bayesian inference-based approach," *IEEE Trans. Wireless Commun.*, vol. 16, no. 11, pp. 7590–7602, 2017.
- [9] L. Lian, A. Liu, and V. K. N. Lau, "Exploiting dynamic sparsity for downlink FDD-massive MIMO channel tracking," *IEEE Trans. Signal Process.*, vol. 67, no. 8, pp. 2007–2021, 2019.
- [10] C. Hu, L. Dai, T. Mir, Z. Gao, and J. Fang, "Super-resolution channel estimation for mmwave massive MIMO with hybrid precoding," *IEEE Trans. Veh. Technol.*, vol. 67, no. 9, pp. 8954–8958, 2018.
- [11] Y. Tsai, L. Zheng, and X. Wang, "Millimeter-wave beamformed full-dimensional MIMO channel estimation based on atomic norm minimization," *IEEE Trans. Commun.*, vol. 66, no. 12, pp. 6150–6163, 2018.
- [12] M. Cui and L. Dai, "Channel estimation for extremely large-scale MIMO: Far-field or near-field?" *IEEE Trans. Commun.*, vol. 70, no. 4, pp. 2663–2677, 2022.
- [13] X. Zhang, H. Zhang, and Y. C. Eldar, "Near-field sparse channel representation and estimation in 6G wireless communications," *IEEE Trans. Commun.*, vol. 72, no. 1, pp. 450–464, 2024.
- [14] H. Hou, X. He, T. Fang, X. Yi, W. Wang, and S. Jin, "Beam-delay domain channel estimation for mmWave XL-MIMO systems," *IEEE J. Sel. Topics Signal Process.*, vol. 18, no. 4, pp. 646–661, 2024.
- [15] S. Liu, X. Yu, Z. Gao, and D. W. K. Ng, "DPSS-based codebook design for near-field XL-MIMO channel estimation," in *ICC 2024 - IEEE International Conference on Communications*, 2024, pp. 3864–3870.
- [16] H. Wu, L. Lu, and Z. Wang, "Near-field channel estimation in dual-band XL-MIMO with side information-assisted compressed sensing," *IEEE Trans. Commun.*, vol. 73, no. 2, pp. 1353–1366, 2025.
- [17] Y. Chen and L. Dai, "Non-stationary channel estimation for extremely large-scale MIMO," *IEEE Trans. Wireless Commun.*, vol. 23, no. 7, pp. 7683–7697, 2024.
- [18] Y. Chen, M. Jian, and L. Dai, "Channel estimation for RIS assisted wireless communications: Stationary or non-stationary?" *IEEE Trans. Signal Process.*, vol. 72, pp. 3776–3791, 2024.
- [19] Z. Lu, Y. Han, S. Jin, and M. Matthaiou, "Near-field localization and channel reconstruction for ELAA systems," *IEEE Trans. Wireless Commun.*, vol. 23, no. 7, pp. 6938–6953, 2024.
- [20] Y. Zheng, M. Zhang, B. Teng, and X. Yuan, "Scalable near-field localization based on array partitioning and angle-of-arrival fusion," in *ICC 2024 - IEEE International Conference on Communications*, 2024, pp. 4415–4420.
- [21] W. Xu, A. Liu, M.-j. Zhao, and G. Caire, "Joint visibility region detection and channel estimation for XL-MIMO systems via alternating MAP," *IEEE Trans. Signal Process.*, vol. 72, pp. 4827–4842, 2024.
- [22] A. Tang, J.-B. Wang, Y. Pan, W. Zhang, X. Zhang, Y. Chen, H. Yu, and R. C. de Lamare, "Joint visibility region and channel estimation for extremely large-scale MIMO systems," *IEEE Trans. Commun.*, vol. 72, no. 10, pp. 6087–6101, 2024.
- [23] Y. Han, S. Jin, C.-K. Wen, and T. Q. S. Quek, "Localization and channel reconstruction for extra large RIS-assisted massive MIMO systems," *IEEE J. Sel. Topics Signal Process.*, vol. 16, no. 5, pp. 1011–1025, 2022.
- [24] C. Han, Y. Wang, Y. Li, Y. Chen, N. A. Abbasi, T. Kürner, and A. F. Molisch, "Terahertz wireless channels: A holistic survey on measurement, modeling, and analysis," *IEEE Commun. Surveys Tuts.*, vol. 24, no. 3, pp. 1670–1707, 2022.
- [25] 3GPP, "Study on channel model for frequencies from 0.5 to 100 GHz (Release 18)," 3GPP, Tech. Rep. 38.901 V18.0.0, May. 2024.
- [26] A. Tang, J.-B. Wang, Y. Pan, W. Zhang, Y. Chen, H. Yu, and R. C. de Lamare, "Line-of-sight extra-large MIMO systems with angular-domain processing: Channel representation and transceiver architecture," *IEEE Trans. Commun.*, vol. 72, no. 1, pp. 570–584, 2024.
- [27] Z. Yuan, J. Zhang, V. Degli-Esposti, Y. Zhang, and W. Fan, "Efficient ray-tracing simulation for near-field spatial non-stationary mmwave massive MIMO channel and its experimental validation," *IEEE Trans. Wireless Commun.*, vol. 23, no. 8, pp. 8910–8923, 2024.
- [28] H. Miao, P. Tang, W. Zuo, Q. Wei, L. Tian, and J. Zhang, "Analysis of near-field effects, spatial non-stationary characteristics based on 11–15 GHz channel measurement in indoor scenario," in *2024 IEEE 25th International Workshop on Signal Processing Advances in Wireless Communications (SPAWC)*, 2024, pp. 231–235.
- [29] Z. Yuan, J. Zhang, Y. Ji, G. F. Pedersen, and W. Fan, "Spatial non-stationary near-field channel modeling and validation for massive MIMO systems," *IEEE Trans. Antennas Propag.*, vol. 71, no. 1, pp. 921–933, 2023.
- [30] L. Qiao, A. Liao, Z. Li, H. Wang, Z. Gao, X. Gao, Y. Su, P. Xiao, L. You, and D. W. K. Ng, "Sensing user's activity, channel, and location with near-field extra-large-scale MIMO," *IEEE Trans. Commun.*, vol. 72, no. 2, pp. 890–906, 2024.
- [31] J. G. Proakis and D. G. Manolakis, *Digital signal processing (3rd ed.): principles, algorithms, and applications*. USA: Prentice-Hall, Inc., 1996.
- [32] J. Zhu, K. Liu, Z. Wan, L. Dai, T. J. Cui, and H. V. Poor, "Sensing RISs: Enabling dimension-independent CSI acquisition for beamforming," *IEEE Trans. Inf. Theory*, vol. 69, no. 6, pp. 3795–3813, 2023.
- [33] M. Liu, M. Li, R. Liu, and Q. Liu, "Dynamic hybrid beamforming designs for ELAA near-field communications," *IEEE J. Sel. Areas Commun.*, vol. 43, no. 3, pp. 644–658, 2025.
- [34] W. Xiao, X. Huang, F. He, J. Silva, S. Emrani, and A. Chaudhuri, "Online robust principal component analysis with change point detection," *IEEE Trans. Multimedia*, vol. 22, no. 1, pp. 59–68, 2020.
- [35] M. Cui and L. Dai, "Near-field wideband beamforming for extremely large antenna arrays," *IEEE Trans. Wireless Commun.*, vol. 23, no. 10, pp. 13 110–13 124, 2024.
- [36] L. Liyang, M. Ke, W. Yue, and W. Zhaocheng, "Near-field communications with block-dominant compressed sensing: Fundamentals, approaches, and future directions," arXiv:2403.12369 [eess.SP], 2025. [Online]. Available: <https://doi.org/10.48550/arXiv.2403.12369>
- [37] Y. Zhang, Z. Zhu, and Y. Xia, "Block sparse bayesian learning: A diversified scheme," in *Advances in Neural Information Processing Systems*, vol. 37. Curran Associates, Inc., 2024, pp. 129 988–130 017.
- [38] J. Rodríguez-Fernández, N. González-Prelcic, K. Venugopal, and R. W. Heath, "Frequency-domain compressive channel estimation for frequency-selective hybrid millimeter wave MIMO systems," *IEEE Trans. Wireless Commun.*, vol. 17, no. 5, pp. 2946–2960, 2018.
- [39] H. Lu and Y. Zeng, "Communicating with extremely large-scale array/surface: Unified modeling and performance analysis," *IEEE Trans. Wireless Commun.*, vol. 21, no. 6, pp. 4039–4053, 2022.